Science Advances
AAAS

advances.sciencemag.org/cgi/content/full/6/23/eaaz7651/DC1

Supplementary Materials for

Cryo-EM structure of NPF-bound human Arp2/3 complex and activation mechanism

Austin Zimmet, Trevor Van Eeuwen, Malgorzata Boczkowska, Grzegorz Rebowski, Kenji Murakami, Roberto Dominguez*

*Corresponding author. Email: droberto@pennmedicine.upenn.edu

Published 5 June 2020, *Sci. Adv.* **6**, eaaz7651 (2020)
DOI: 10.1126/sciadv.aaz7651

The PDF file includes:

Figs. S1 to S9
Table S1
Legend for movie S1

Other Supplementary Material for this manuscript includes the following:

(available at advances.sciencemag.org/cgi/content/full/6/23/eaaz7651/DC1)

Movie S1

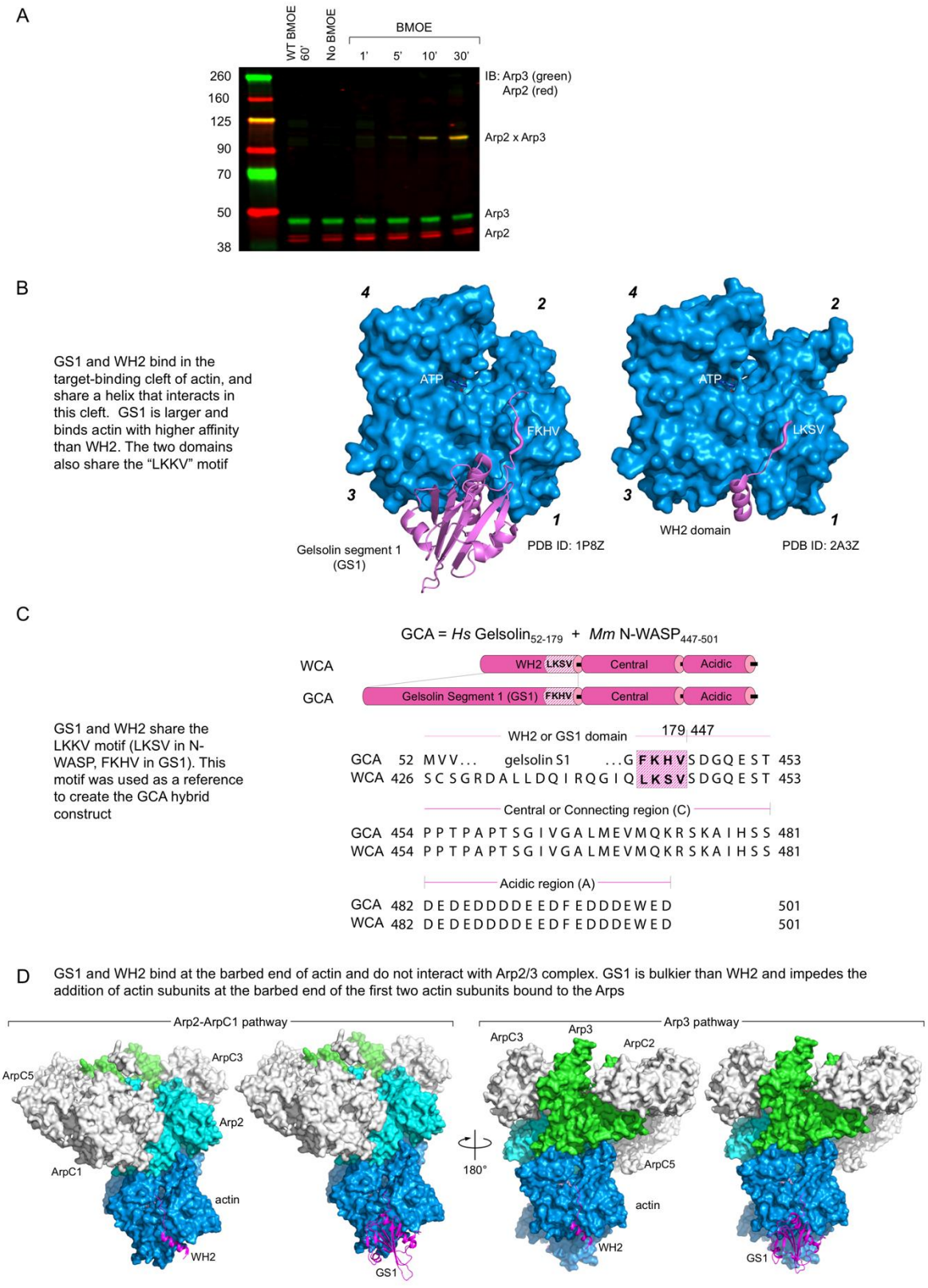

fig. S1. Crosslinking reaction and replacement of the WH2 domain of WCA with GS1. (**A**) Two-color Western blot analysis (Arp2, red; Arp3, green) of Arp2/3 complex diCys mutant treated with BMOE for the indicated amounts of time. Controls include WT human Arp2/3 complex treated with BMOE for 60 min and untreated diCys mutant. (**B**) Both, the WH2 domain

and gelsolin segment-1 (GS1) bind at the barbed end of the actin monomer and insert a helix in the hydrophobic cleft formed between actin subdomains 1 and 3 (*35*). Both domains also share the LKKV motif (*2*) (FKHV in GS1 and LKSV in N-WASP). (**C**) Schematic representation and sequence of GCA compared to N-WASP WCA, highlighting the location of the LKKV motif used as reference for fusion of the two proteins (*25*). (**D**) Whether the first actin subunit binds at the barbed end of Arp2 or Arp3, the WH2 to GS1 substitution does not influence the conformation of Arp2/3 complex, since the CA region, but not the WH2 domain contacts Arp2/3 complex (*14, 16*), as these models illustrate. GS1 binds actin stably and with higher affinity than WH2 (*17, 31*), such that the actin-GCA complex can be pre-purified, avoiding the presence of free actin monomers in solution. GS1 is also bulkier than WH2, such that GCA sterically impedes the binding of additional actin subunits, effectively trapping the nucleation reaction after actin-GCA binding and delivery of the first two actin subunits to Arp2 and Arp3.

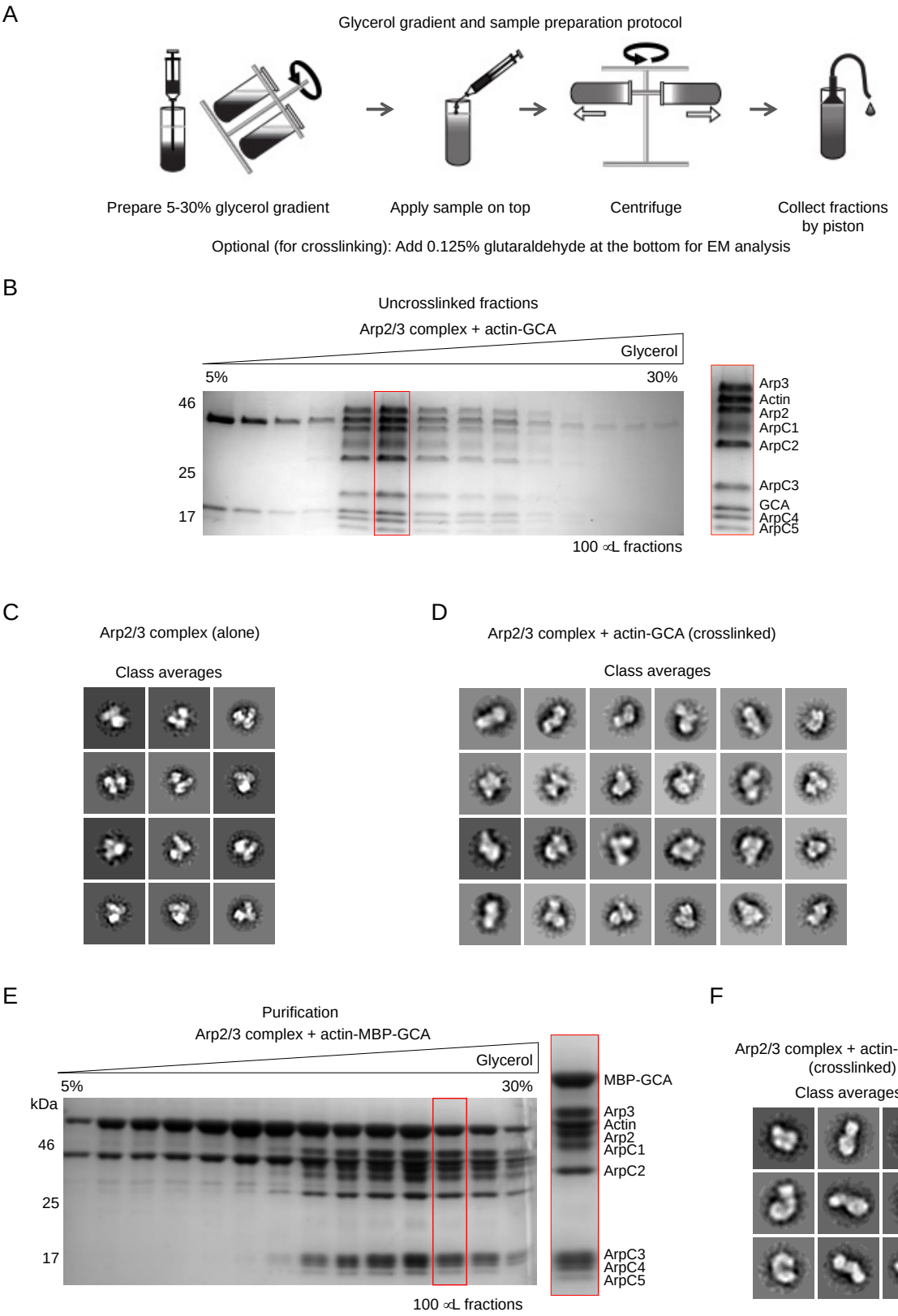

fig. S2. EM characterization of Arp2/3 complex ± actin-GCA or actin-MBP-GCA. (**A**) Description of the glycerol gradient and glutaraldehyde crosslinking protocol (GraFix) used to obtain a 1:1:1 actin:GCA:Arp2/3 complex for EM analysis of negatively-stained specimens. (**B**) SDS-PAGE analysis of glycerol gradient fractions of human Arp2/3 complex (5 µM) with a 3-

fold molar excess actin-GCA in the absence of crosslinking agent. The inset highlights the peak fraction used for EM analysis (with crosslinking) or for biochemical analysis (without crosslinking, see Fig. 2, A and B). (**C**) Representative 2D class averages of bovine Arp2/3 complex alone. (**D**) Representative 2D class averages of crosslinked 1:1:1 actin:GCA:Arp2/3 complex. (**E**) SDS-PAGE analysis of glycerol gradient fractions of bovine Arp2/3 complex (5 μM) with a 3-fold molar excess actin-MBP-GCA in the absence of crosslinking agent. The inset highlights the peak fraction used for EM analysis (with crosslinking). (**F**) Representative 2D class averages of crosslinked 1:1:1 actin:MBP-GCA:Arp2/3 complex.

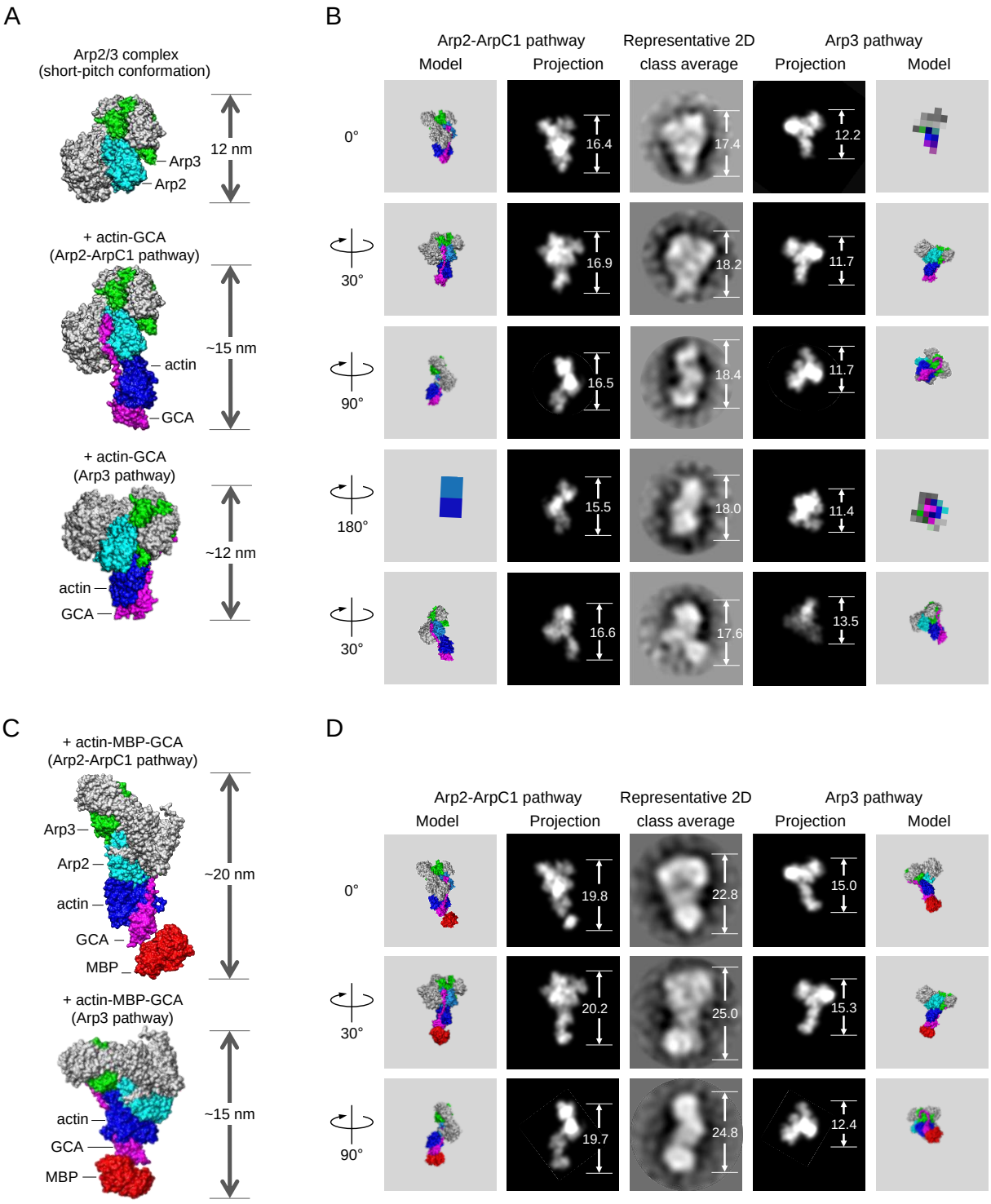

fig. S3. The high-affinity actin-NPF-binding site is on Arp2-ArpC1. (**A**) Models of Arp2/3 complex in the short-pitch conformation (obtained by moving Arp2 alongside Arp3, analogous to two adjacent subunits of the actin filament), and actin-GCA at the barbed end of Arp2 (Arp2-ArpC1 pathway) or Arp3 (Arp3 pathway). Note that these models have different overall topologies and substantially different dimensions. (**B**) EM analysis and 2D class averages of crosslinked bovine Arp2/3 complex with bound actin-GCA. Left to right: best scoring orientation

of the Arp2-ArpC1 pathway model, 2D projection of the best-scoring Arp2-ArpC1 pathway model, representative 2D class average corresponding to this orientation, 2D projection of the best-scoring Arp3 pathway model, and best-scoring orientation of the Arp3 pathway model. Maximum dimensions listed for comparisons (unit: nm). The best-scoring projections were generated with the EMageFit protocol of the Integrative Modeling Platform suite (*43*). (**C**) Models of Arp2/3 complex in the short-pitch conformation with actin-MBP-GCA at the barbed end of Arp2 (Arp2-ArpC1 pathway) or Arp3 (Arp3 pathway). (**D**) EM analysis and 2D class averages of crosslinked Arp2/3 complex with bound actin-MBP-GCA (shown as described in part B). The orientations shown correspond to the first three orientations in part B.

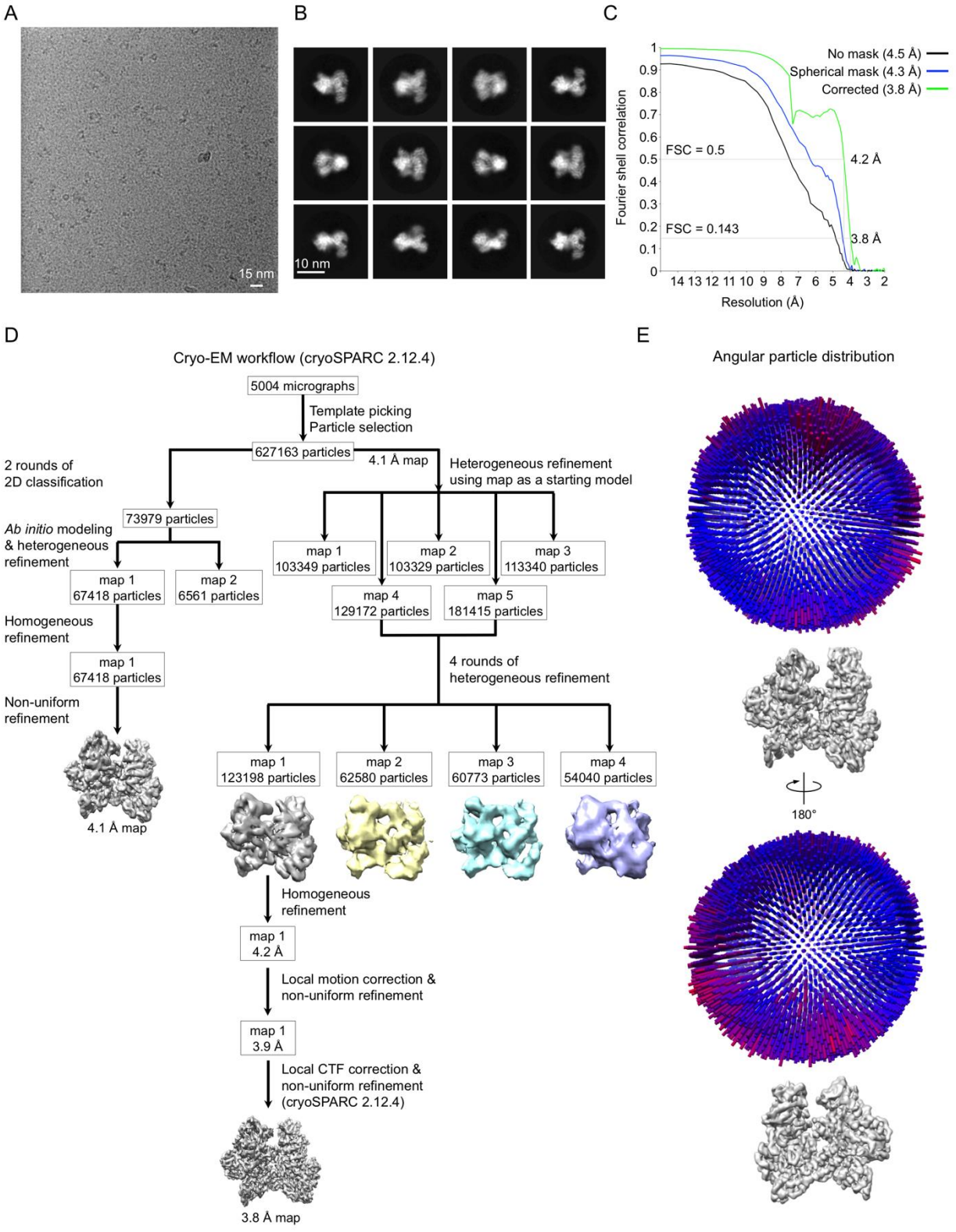

fig. S4. Cryo-EM image processing and workflow. (**A**) Representative electron micrograph. (**B**) Representative 2D class averages obtained from reference-free 2D classification with cryoSPARC v2.12.4. (**C**) Fourier shell correlation (FSC) curves obtained from the final non-uniform refinement with cryoSPARC. The resolution is estimated at FSC = 0.143 and 0.5 (**D**) Summary of

data processing procedures and workflow. (**E**) Euler plot distribution of particle views in the final reconstruction, where the view representation increases from blue to red.

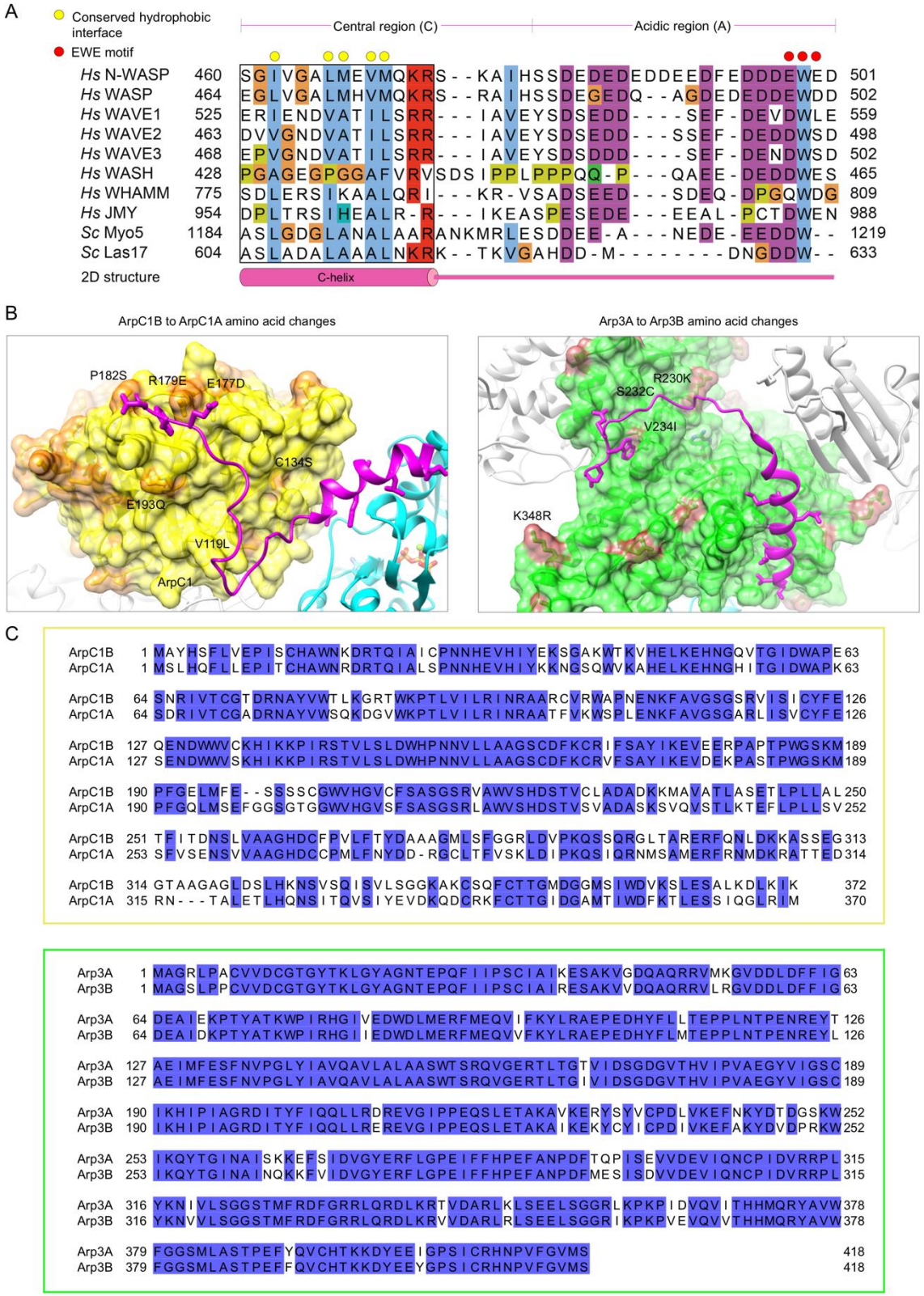

fig. S5. Sequence variation of the WCA region of NPFs and among Arp2/3 complex isoforms. (**A**) Sequence alignment of the CA region of various human and budding yeast NPFs (as indicated). The most highly conserved elements include the hydrophobic face of the amphipathic C-helix (yellow circles) and the C-terminal ^{498}EWE^{500} motif (red circles). These

conserved elements are better defined in the cryo-EM map (Fig. 3). The only secondary structural element of the CA region is the C-helix (2D structure at the bottom of the alignment). While the abundance of negatively-charged amino acids in the D/E-loop is also conserved among NPFs, the length of this loop varies from 18 to 24 amino acids in WAVE3 and N-WASP, respectively. The D/E-loop is less well defined in the cryo-EM map. (**B**) Surface representation of ArpC1B (left, yellow) and Arp3 (right, green) highlighting side chain variations between isoform (orange-colored amino acids). The CA of N-WASP is shown in magenta. (**C**) Sequence alignment of the human Arp2/3 complex isoforms of ArpC1 (top) and Arp3 (bottom). The structure determined here contains isoforms ArpC1B and Arp3A.

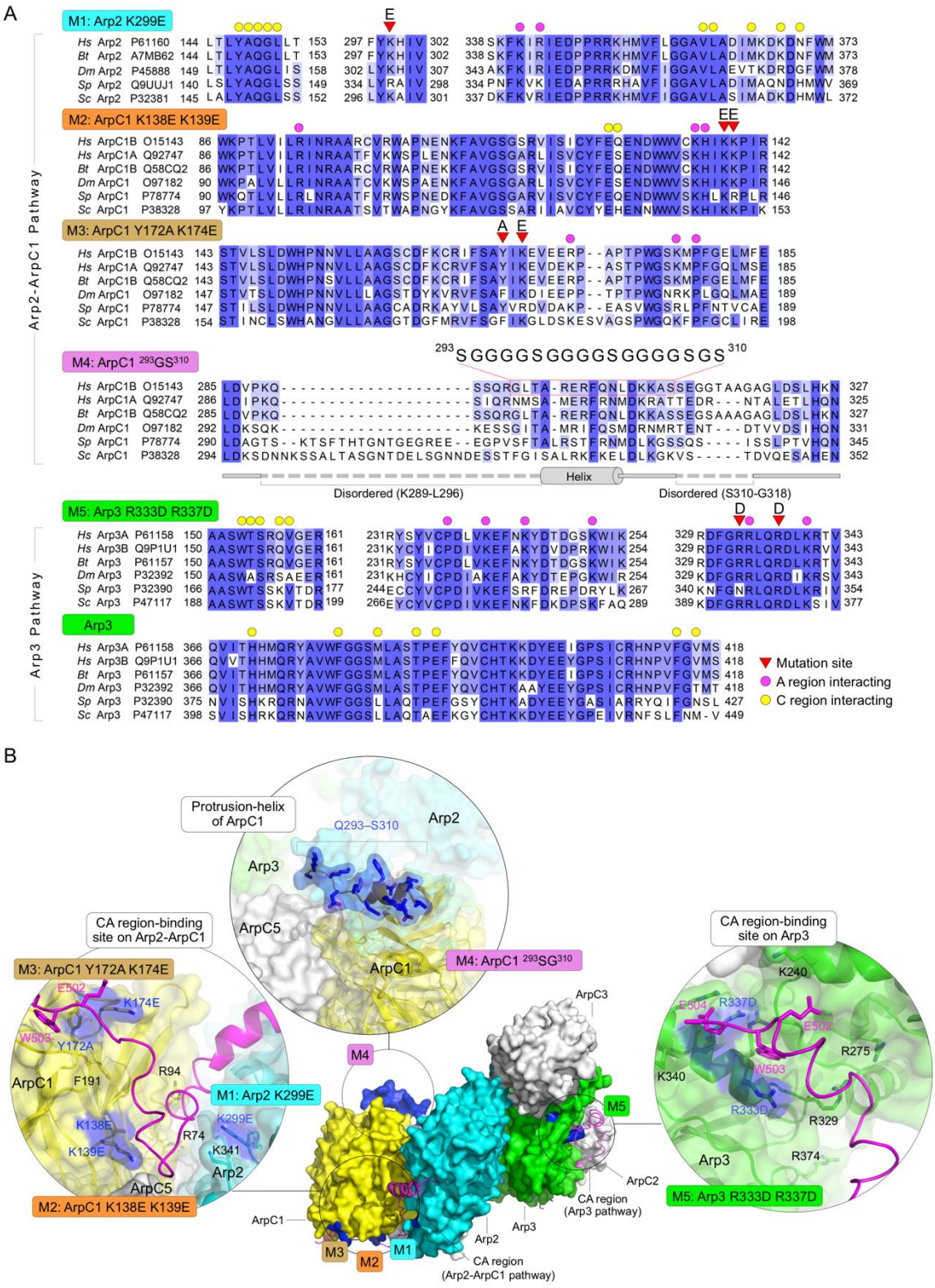

fig. S6. Description of the human Arp2/3 complex mutants. (**A**) Sequence alignments of different species and isoforms of Arp2, ArpC1 and Arp3, highlighting the amino acids that were replaced in human Arp2/3 complex mutants M1-M5 (red arrowheads on top of the alignment). The mutants are color-coded (see also Figs. 5 and 6 and figs S7 and S8). Other amino acids implicated in interactions with the C and A regions of N-WASP are indicated by yellow and

magenta circles, respectively. (**B**) Illustrations of mutants M1-M5 on the cryo-EM structure of human Arp2/3 complex. Subunits are labeled and colored: Arp2 (cyan), ArpC1 (yellow), Arp3 (green) and ArpC2-ArpC5 (gray). The two N-WASP CA polypeptides are colored magenta. Insets show close-up views of the mutated amino acids (blue).

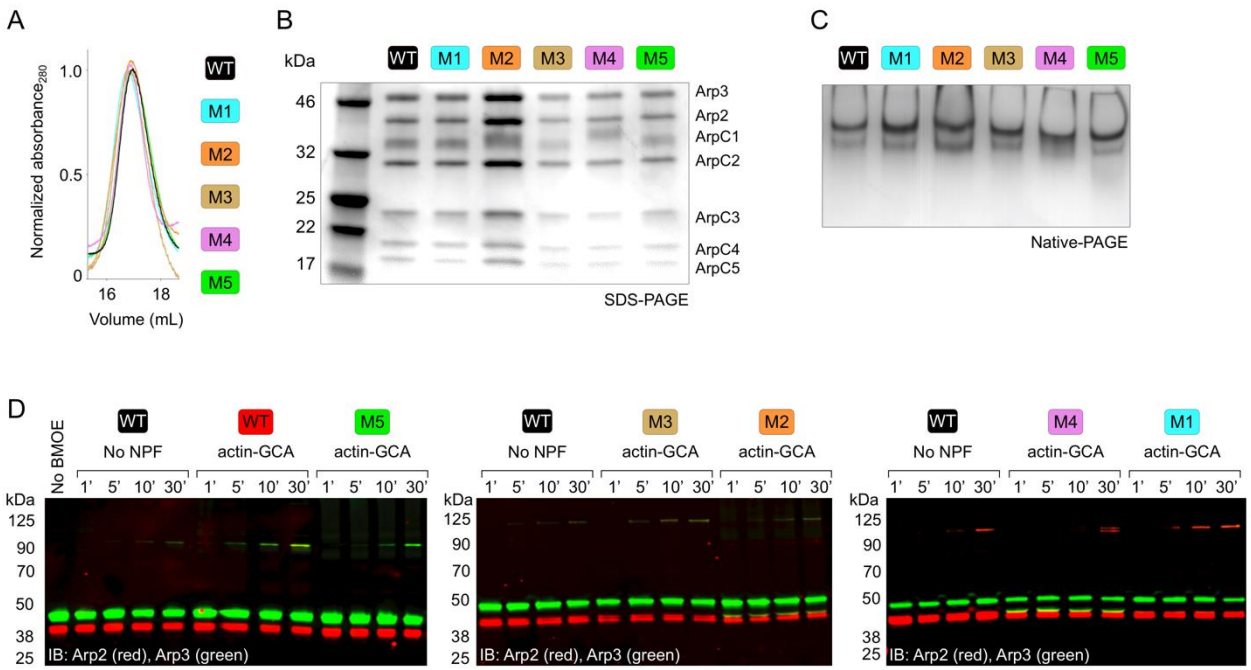

fig. S7. Analysis of human Arp2/3 complex mutants. (**A**) Comparison of the Superose 6 size exclusion profiles of human Arp2/3 complex WT and mutants M1 to M5 (color-coded), showing similar retention volumes. (**B, C**) SDS-PAGE and native-PAGE analysis of purified Arp2/3 complex WT and mutants, showing similar migration patterns. (**D**) Two-color Western blot analysis (Arp2, red; Arp3, green) of crosslinking reactions of diCys Arp2/3 complex (called here WT for simplicity) and mutants M1-M5 (generated in the background of the diCys mutant) in the presence or the absence of actin-GCA and at different BMOE treatment times (as indicated). BMOE untreated diCys mutant (WT) is also shown as a control.

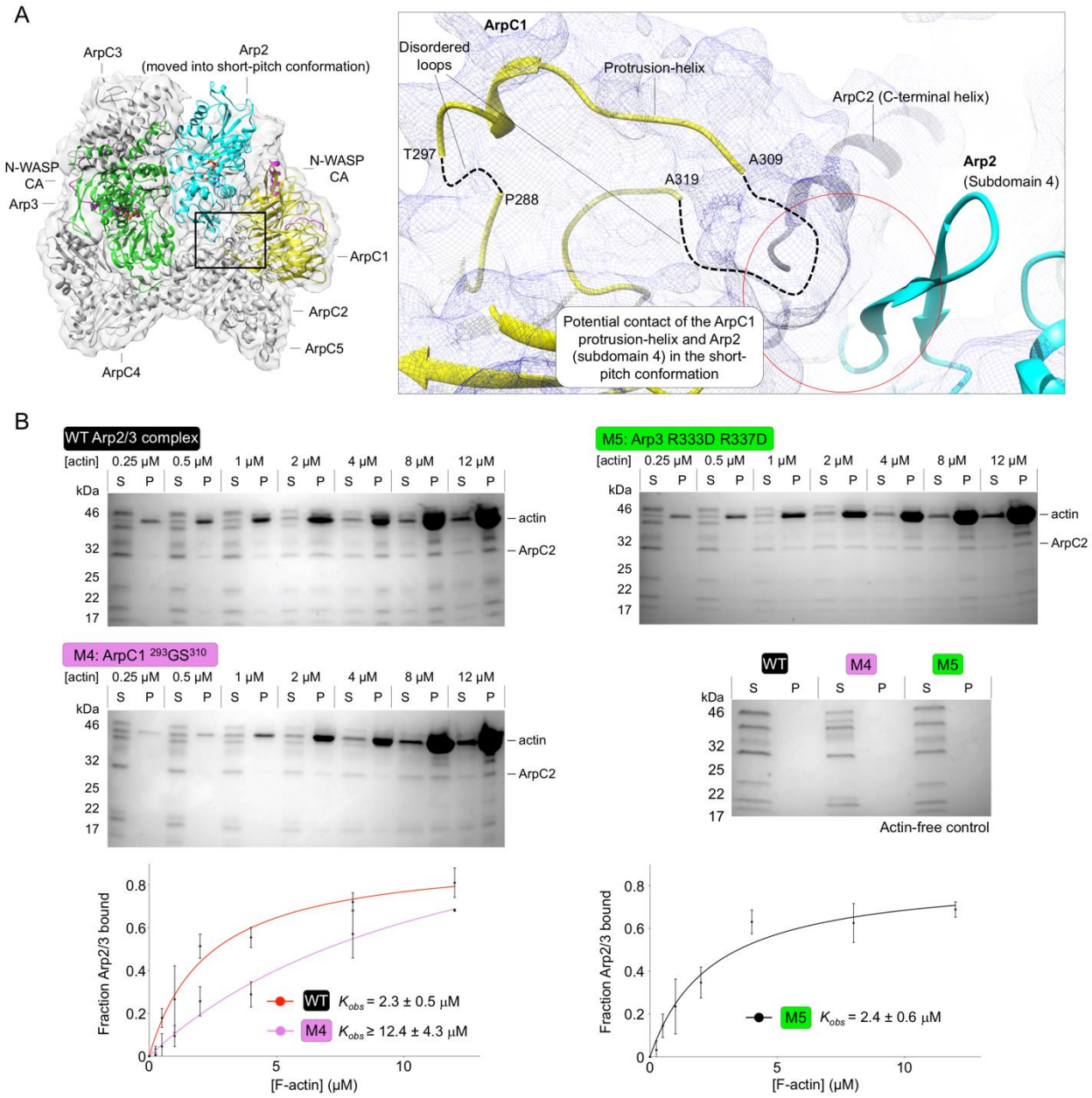

fig. S8. Potential role of the ArpC1 protrusion-helix in Arp2/3 complex activation. (**A**) When Arp2 is moved into a short-pitch conformation, subdomain 4 likely contacts the protrusion-helix of ArpC1, shown here as the poorly-defined loop-helix-loop region between P288 and A319, which appears in the cryo-EM map (inset, blue grid) when it is contoured at a lower signal to noise level (6 σ). This contact may explain why mutant M4 (targeting the protrusion-helix) affects the short-pitch transition, although it does not participate in interactions with the NPFs. The C-terminus of subunit ArpC2 also falls in this density. (**B**) SDS-PAGE analysis and quantification of cosedimentation assays of WT and mutants M4 and M5 (control for this experiment) as a function of F-actin concentration. Note that the complex and mutants are soluble and do not sediment in the absence of F-actin. The bound fraction of Arp2/3 complex was determined by densitometric analysis of the ArpC2 band in the pellet (P) vs. the supernatant (S) fractions (n=3). The observed

dissociation constant (K_{obs}) was calculated using a non-linear least square fit. According to this analysis, M4 has lower affinity for F-actin that the controls (WT and M5), suggesting that the protrusion helix in ArpC1 participates in interactions with the mother filament.

A

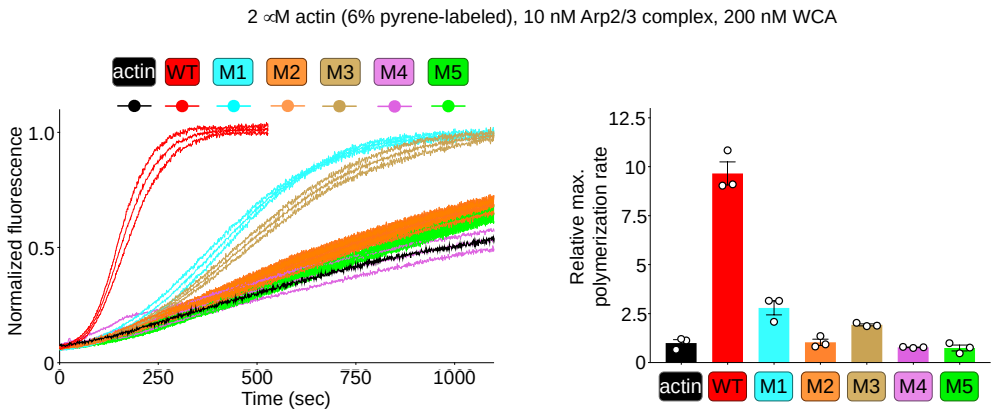

B

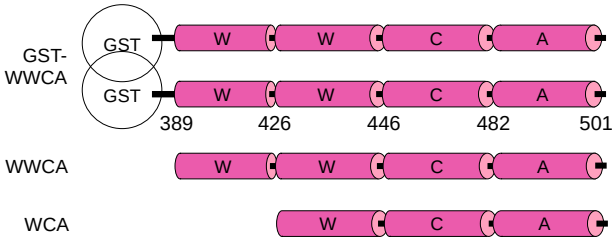

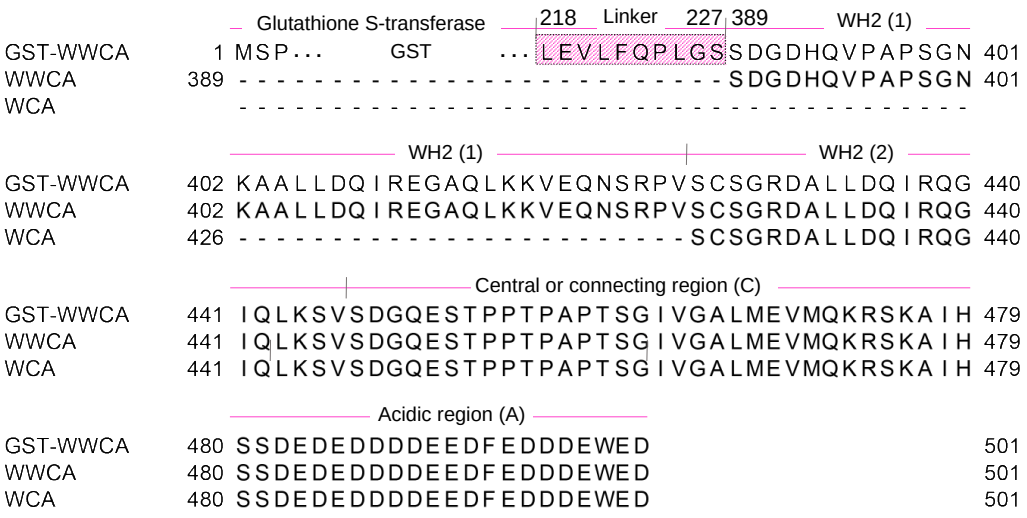

fig. S9. Distinct roles of the two NPF-binding sites of Arp2/3 complex. (**A**) (Left) Time-course of actin polymerization by WT and mutant human Arp2/3 complex variants (as indicated) under the conditions listed above the figure. (Right) Relative polymerization rates calculated by determining the first derivative of the curve and normalizing the maximum derivative value to that of actin alone (n=3). (**B**) Schematic (top) and sequence (bottom) description of mouse N-WASP constructs WWCA (residues 389-501) and GST-WWCA (dimeric). Note that a 10-aa linker connects the N-terminal GST to WWCA (striped region).

Table S1. Cryo-EM data collection and model building

Human Arp2/3 complex with two bound N-WASP WCA region

Data collection and processing	
Magnification	165,000x
Voltage (kV)	300
Electron exposure (e–/Å^2)	40
Defocus range (μm)	-1.75 to -3.5
Pixel size (Å)	0.418
Symmetry imposed	C1
Initial particle images (no.)	627,163
Final particle images (no.)	123,198
Map resolution (Å)	3.8 (FSC threshold 0.143)
Map resolution range (Å)	3.0-8.5
Model building	
Initial search model	*Ab initio*, CryoSPARC
Fitting model (PDB code)	4JD2
Map sharpening B factor (Å^2)	-131.5
Model composition	
Non-hydrogen atoms	14,680
Protein residues	1,940
Ligand atoms	64
R.M.S. deviations	
Bond lengths (Å)	0.008
Bond angles (°)	1.366
Validation	
MolProbity score	2.10
Clash score	12.15
Poor rotamers (%)	5.76
Ramachandran plot	
Favored (%)	91.61
Allowed (%)	7.19
Outliers (%)	0.21
EMDB accession code	20770
PDB accession code	6UHC

Movie S1. Cryo-EM structure of human Arp2/3 complex with bound N-WASP CA. The first part of the movie shows the cryo-EM map and the second part shows the difference map for the two CA polypeptides bound.